Calibration of Concentric Tube Continuum Robots: Automatic Alignment of Precurved Elastic Tubes

Vincent Modes[1], and Jessica Burgner-Kahrs[2], *Senior Member, IEEE*

***Abstract*—Joint level calibration is an integral part of robotics as it directly influences the achievable accuracy. As opposed to serial robotic arms, continuum robots are not composed of any rigid links or joints, but of elastic materials that undergo bending and torsion. The jointless composition requires dedicated calibration procedures.**

In this paper, we introduce an automatic method for aligning precurved elastic tubes for joint level calibration of concentric tube continuum robots. The robot tip is equipped with a sensor in order to track its position during calibration such that subsequent data processing can extract the rotational zero position automatically. While we present a general framework independent of the utilized sensor technology, we evaluate our approach using three different sensing methodologies, i.e. magnetic, inductive, and electromagnetic. Furthermore, we advise on properties for appropriate sensors. Our experimental results show, that the rotational home position can be found reproducibly with a minimal dispersion of 0.011 °.

***Index Terms*—Flexible Robots, Calibration and Identification**

I. Introduction

CALIBRATION is an integral part in robot applications, whether serial [1], parallel [2] or mobile [3] robots are concerned. It improves robot accuracy (i.e. how well a measured robot pose confirms with the expected pose calculated by the kinematic model) and assures, that the robot reaches its commanded destination reproducibly even after several performed calibration procedures.

As opposed to conventional serial or parallel robots, continuum robots are composed of elastic materials such that their body conforms to a continuous shape [4][5]. Concentric tube continuum robots (CTCR) are the smallest kind of continuum robots existing today. They are composed of several precurved tubes made of superelastic materials, such as Nitinol, which are nested inside one another. By rotating and translating the tubes at their bases with respect to each other, the elastic interactions lead to complex tentacle-like motions of the CTCR. Their small size (outer diameter $<$1 mm), their inherent elasticity as well their unique motion behavior make them well suited for applications in confined spaces (e.g. minimally-invasive surgery), but also make them challenging to control. Current model-free kinematics depend on extensive data collections [6] which makes them impractical for applications demanding quick tube replacement and fast setup times [5]. While model-based approaches need less data, the jointless structure and composition of precurved tubes require special consideration for calibration methods.

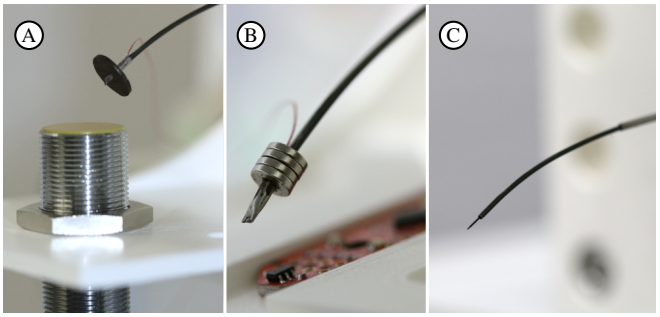

Fig. 1. Sensors for calibration: inductive (A), magnetic (B), electromagnetic (C) (field generator not shown)

A. Related work

Roth et al. [7] specify three levels for calibration of conventional serial robot kinematics. Level 1 calibration (also called *joint level calibration*) aims to relate the readouts from the joint encoders with the real displacement of the joint as well as to determine the correct start value for the encoder reading (also known as home or zero position). Level 2 calibration aims to adjust all relevant parameters for the kinematic calculation and incorporates Level 1 calibration. In general, Roth et al. consider rigid body kinematics with stiff links and joints without clearance. The purpose of Level 2 calibration is to find the geometric kinematic parameters, such as link length or angular relationships between links. It is also referred to as *geometric calibration*. Parameters that are not part of the geometric model (e.g. link and joint compliance, friction, clearance) can be determined in Level 3 calibration. This also includes parameters affecting the dynamic model of the robot. Level 3 calibration is also denoted as *non-geometric calibration*.

Geometric calibration of continuum robots is design specific. Most commonly, it is assumed that the individual segments of a continuum robot bend with constant curvature. Escande et al. [8] calibrate a pneumatically actuated continuum robot consisting of two consecutive bendable segments using

Manuscript received June 04, 2019; Revised August 28, 2019; Accepted September 27, 2019.

This paper was recommended for publication by Editor Dezhen Song upon evaluation of the Associate Editor and Reviewers' comments. This work was supported by the German Research Foundation under award number BU 2935/1-1.

[1]Vincent Modes is affiliated with the Institute of Mechatronic Systems, Leibniz Universität Hannover, Hanover, Germany vincent.modes@imes.uni-hannover.de

[2]Jessica Burgner-Kahrs is affiliated with the Department of Mathematical & Computational Sciences, University of Toronto, Canada jessica.burgnerkahrs@utoronto.ca

Both authors have previously been affiliated with the Laboratory for Continuum Robotics, Leibniz Universität Hannover, Hanover, Germany

Digital Object Identifier (DOI): see top of this page.

external potentiometers to measure tip positions in order to identify geometric parameters of the kinematics.

Advanced kinematic models are based on continuum mechanics in order to incorporate material properties of the robot structure such as material elasticity or stiffness [5]. These parameters can be determined before the robot assembly as e.g. proposed in Dehghani and Moosavian [9] or Deutschmann et al. [10] using elaborate measurement setups. More commonly, the calibration of continuum robots is performed on the assembled manipulator. A Level 2 calibration methodology for multibackbone continuum robots using a kinematics framework which accounts for captured joint space errors due to homing offsets, assembly errors causing twist about the robot's backbone, and uncertainty in the equilibrium bending shapes of robot segments was introduced by Wang and Simaan [11].

Chikhaoui et al. [12] calibrated an extensible, multi-segment tendon-actuated robot. By minimizing the deviation between the robot's tip position (measured with a laser scanner) and the estimate of the forward kinematic model, they identify the robot's Young's modulus, stiffness of bendable structural robot parts, coefficients of a tendon elongation model and the pose of the robot's base frame in the world coordinate system. Furthermore, the length of each section in the robot's home position is measured with a caliper.

So far, calibration procedures for CTCR have been investigated sparsely. Webster et al. [13][14] calibrate a CTCR under constant curvature assumptions including torsion in the transmission. Rucker et al. [15] calibrate a generalized CTCR model. These methods identify kinematic parameters and material properties such as Young's modulus, moment of inertia, and Poisson's ratio. Other calibrated parameters are the transformation between the robots base frame and an external measurement system, the position of markers attached to the robot as well as the angle under which the robot exits its base plate [16].

These calibration methods for CTCR can be classified as Level 2 calibration, excluding joint level calibration. To the best of our knowledge, the determination of the rotational and translational zero position of CTCR has not been explicitly regarded in the state of the art.

B. Motivation

We investigate CTCR composed of tubes with planar constant precurvatures, which may have a straight segment preceding the curved segment. The reference position (also referred to as zero or home position) is the robot pose in task space that defines the zero value for the kinematic configuration parameters in configuration space. For CTCR the configuration parameters are defined for each tube i as the rotation angle α_i around the z-axis and the translational distance with respect to the robot base β_i (see Fig. 2). i is incremented in outward radial direction starting at 1.

To investigate the influence of the deviations in the zero position for α_i and β_i we perform a global variance-based sensitivity analysis [17]. Using a Cosserat rod model [18], we simulate a CTCR consisting of three tubes with Young's modulus of 50 GPa and a Poisson's ratio of 0.3. The specific parameters

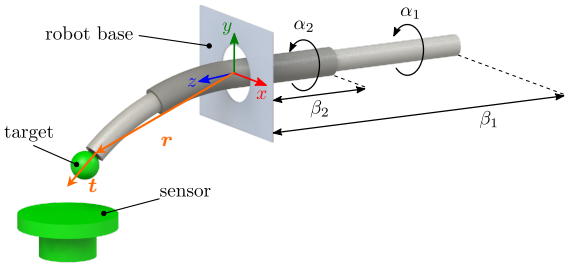

Fig. 2. Two-tube CTCR with exemplary target and sensor. The robot base frame lies in the base plate. α_i is the rotation angle of tube i around the z-axis and β_i denotes the translational distance of the tube end from the base plate. $\boldsymbol{r}$ is the robot's tip position vector and $\boldsymbol{t}$ the tip tangent vector.

of tube $i = (1/2/3)$ are: outer diameter of (1.14/1.78/2.18) mm, inner diameter of (0.75/1.20/2.05) mm, straight length of (439/280/145) mm, curved length of (66/62/30) mm and precurvature of (9.53/3.63/2.08) m^{-1}.

The nominal rotational and translational position α_i and β_i are assumed to be prone to small offsets $\Delta\alpha_i \in [-5, 5]^\circ$ and $\Delta\beta_i \in [-3, 3]\mathrm{mm}$ caused by an inaccurate calibration. We compare the tip position $\boldsymbol{r}$ and the tip tangent vector $\boldsymbol{t}$ (see Fig. 2) of an ideal model with the values of a model suffering from an imperfect calibration, which is denoted by the superscript *. Hence, we define the tip position error as $||\boldsymbol{r} - \boldsymbol{r}^*||_2$ and the tip orientation error as the angle between $\boldsymbol{t}$ and $\boldsymbol{t}^*$. For 20 random robot configurations, we perform a Monte-Carlo simulation with 5000 samples drawn from a uniform distribution for each $\Delta\alpha_i$ and $\Delta\beta_i$ and calculate the total effects S_T as shown in Fig. 3.

S_T reflects the individual influence of a specific parameter including every interaction between this and the other investigated parameters. As expected, the position error is mainly caused by interactions of $\Delta\beta_1$. However, at least for point 18 and 20, also $\Delta\alpha_1$ and $\Delta\alpha_2$ have an influence on the error spreading. Looking at S_T for the orientation error reveals a high interaction between $\Delta\alpha_1, \Delta\alpha_2, \Delta\beta_1$ and $\Delta\beta_2$ while the influence of $\Delta\alpha_3$ is marginal. The reason of the latter is the small curvature and short length of tube 3 causing comparably small robot tip motions. However, because of the large interactions especially on the tip orientation error, it is not sufficient to solely calibrate β_1 or α_1.

Mostly, the tubes of CTCR are translated by linearly moving carriages. Hence, one can easily determine the translational reference position by attaching limit switches to the robot's actuation unit. However, identification of the reference position for the rotational degree of freedom of each individual tube is not trivial. In fact, common practice is to manually adjust the rotational home position based on visual judgment. If the robot's zero position is not explicitly determined, Level 2 calibration implicitly compensates for offsets in the home position by overadjusting the kinematic parameters. Thus, performing Level 1 calibration beforehand would allow identification of further kinematic coefficients with higher certainty.

C. Contribution

The main contribution of this paper is an efficient method with practical guidelines for automated, tactile free calibration

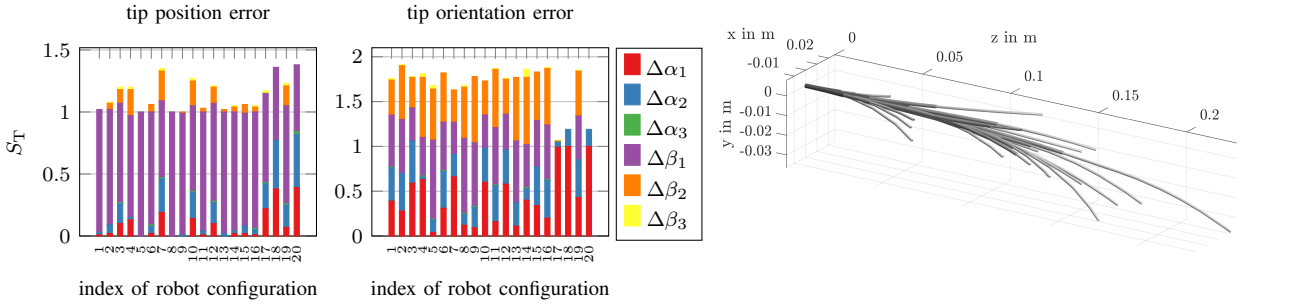

(a) total effects (b) robot configurations

Fig. 3. Resulting total effects S_T of a global variance-based sensitivity analysis (a) calculated with a Monte-Carlo simulation on 20 robot configurations (b) with 5000 samples for each parameter drawn from a uniform distribution.

of the rotational reference position for CTCR. The steps of the procedure are designed such that the Level 1 calibration process can be automated to decrease the robot's setup time. By evaluating the algorithm using different sensors (see Fig. 1), we demonstrate general applicability.

II. Calibration Procedure

A. Assumptions

We define the rotational reference position of a CTCR as the set of α-values such that all tubes point downwards along the negative y-axis with their precurvatures aligned in the y-z-plane as shown in Fig. 2. We seek in finding this position by placing a reference sensor close to the robot such that the distance between the robot's tip (or more precisely a target mounted to the tip) and the sensor has an extremum at exactly this position. Furthermore, we simplify the robot's motion behavior by assuming, that a single tube rotation causes a circular motion of the tube tip in a plane parallel to the x-y-plane of the robot base system. In order to minimize the influence of the tubes on each other, each rotational joint (i.e. every tube) should be calibrated separately. The subscript $_\mathrm{c}$ marks a calibrated configuration value (e.g. α_i is a rotational parameter of tube i while $\alpha_{i,\mathrm{c}}$ is the calibrated rotational home position).

B. Calibration Workflow

The calibration workflow is illustrated in Fig. 4 and composed of the following steps:

S-1 Place sensor in front of or near the robot base
S-2 Attach target to robot's tip
S-3 Adjust sensor position & orientation such that the sensor signal has an extremum at the rotational home position
S-4 Rotate all tubes to point downwards (manual pre-calibration). Use this configuration as a preliminary home position for the α_i values
S-5 Retract all tubes until the robot's tip is positioned as close as possible to the robot base
S-6 Move the innermost uncalibrated tube i as far out as possible to place the target over the sensor
S-7 Rotate target over the sensor by driving α_i from $\alpha_{i,\mathrm{start}}$ to $\alpha_{i,\mathrm{end}}$ and back to $\alpha_{i,\mathrm{start}}$. Collect sensor data $v(t)$ and position data $\alpha_i(t)$ over time t during the motion
S-8 Synchronize sensor and position data to generate $v(\alpha_i)$
S-9 Create two data subsets from $v(\alpha_i)$ by removing constant sensor values (e.g. caused by sensor saturation)
S-10 Fit functions $f_\mathrm{l}(\alpha_i)$ and $f_\mathrm{r}(\alpha_i)$ to the left and right part of the cropped data. Calculate the extrema $\alpha_{i,\mathrm{cl}}$ and $\alpha_{i,\mathrm{cr}}$ of $f_\mathrm{l}(\alpha_i)$ and $f_\mathrm{r}(\alpha_i)$, respectively. The average of these extrema denotes the home position $\alpha_{i,\mathrm{c}}$ of tube i
S-11 Move tube i to $\alpha_{i,\mathrm{c}}$
S-12 Repeat from S-6 until all tubes are calibrated

The adjustments in S-3 are affected by the used sensor. Depending on the physical sensing volume, the final position should assure that no signal saturation occurs at the expected home position. Orienting the sensor axes in parallel to the robot base frame simplifies the determination of the relationship between the sensor signal and the target's position during tube rotation as utilized in section II-D2.

The motion range chosen in S-7 must assure that the robot keeps a sufficient distance to unstable configurations which could lead to undesirable motion behavior also known as *snapping* [19][20]. Furthermore, in each measurement run, the target should pass the sensor from both directions, e.g. the tubes should rotate clockwise and counterclockwise. Due to gear backlash, material torsion, friction as well as clearance between tubes, a difference between the rotation angle of the actuators and the corresponding tube tip occurs [21]. Because this lag is symmetrical with respect to both rotation directions, we balance its negative effect by averaging the calculated extrema as in S-10.

The fit function in S-10 must be chosen depending on the used sensor system. In section II-D2, we provide three exemplary functions suitable for sensors used in our experiments.

C. Sensor Selection

The selection of an appropriate sensor and a corresponding target depends on the intended application. Restrictions of and compatibility with the environment must be considered (e.g. tolerance against electric, magnetic, or electromagnetic fields). In general, the chosen sensing system should be tactile free as even small forces acting on a CTCR may cause deformation. Furthermore, the sensor must deliver a signal that is a continuous function with respect to the distance between the target and the sensor. The maximum and minimum sensing distance should be selected such that the sensor signal shows a

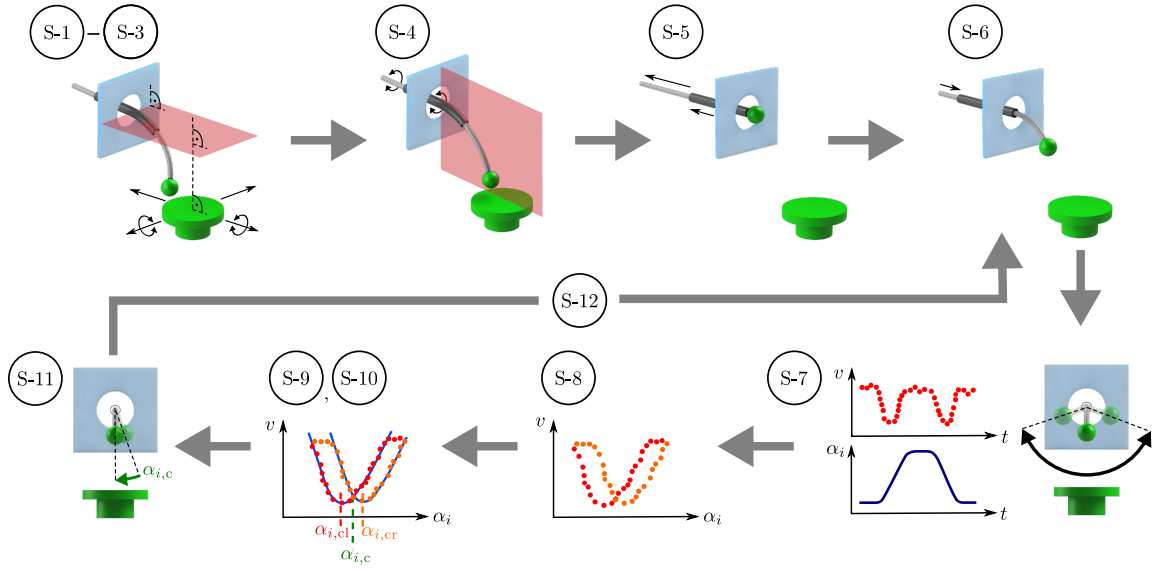

Fig. 4. Calibration workflow: sensor placement (S-1)-(S-3); manual pre-calibration (S-4); tube motion to start position (S-5), (S-6); calibration motion and data collection (S-7); data synchronization (S-8); data processing and calculation of reference position (S-9),(S-10); tube rotation to calibrated position (S-11); repetition from step (S-6) until all tubes are calibrated (S-12)

clear extremum at the reference position (i.e. it does not reach saturation during data collection). This reduces the complexity of the fit function used in S-10. Depending on the pre-curvature of the tubes, the usable sensing distance affects the position at which the sensor can be placed in S-3, the β-values chosen in S-6 as well as the angle of which the tube is rotated in S-7. These values should be chosen in such away, that the value range of $v(t)$ is maximized while saturation is avoided.

Throughout this work, we investigate three exemplary sensor systems based on different sensing principles: a magnetic, an inductive as well as an electromagnetic tracking sensor.

The magnetic sensor uses the Hall effect to measure the components of the magnetic flux density $\boldsymbol{B}$ produced by a permanent magnet mounted on the robot's tip.

The inductive sensor (or eddy current sensor) changes the impedance of the sensor coil if a metallic target is moved in front of the sensor. This affects the frequency of a connected oscillating circuit, which is mapped to a voltage signal. Note, that this signal is only linear, if the target moves along the roll or longitudinal axis of the cylindrical sensor.

The electromagnetic sensor system uses a field generator to create an oscillating electromagnetic field, which induces a voltage in a sensor coil. After measuring this voltage, the coil's position and orientation is calculated by the system and digitally provided to the user.

While all systems deliver a continuous signal as a function of distance between the target and the sensor, the varying functional relationship between the measured data and the target position must be explicitly treated in the following data processing. Using a function whose parameters are related to physical properties of the experimental setup simplifies the determination of start values for the following, numerically solved function fitting.

To formulate a sensor placement guideline, we refer to the definition of the home position from section II-A. The passing of the target through the robot's y-z-plane must cause an extremum in the sensor signal. The most general approach to achieve this (independently if the sensor can measure values in one, two or three directions), is by placing the origin of the sensors measurement coordinate system in the robot's y-z-plane and orient its principal sensing axis (if existent) in the direction of the target's transition point through this plane. Orienting the sensor frame in the same manner as the robot base frame allows for a straight-forward relation of the sensor signal to the target's motion. By taking advantage of the specific characteristics of the different sensor signals, deviating from this recommendation is possible as explained in section III-A for the sensors used in the experiments.

D. Data Processing

After measuring (S-7) and synchronizing (S-8) all data, the calibration position is determined in two steps. First, relevant data for the calibration process is segmented in a preprocessing step (S-9). Afterwards, a sensor specific function is fitted to the data (S-10).

1) Preprocessing: Fig. 5 shows an exemplary measurement series of sensor data v over time t. It can be approximated by alternating series of constant and sinusoidal functions. Relevant for the calibration process is only the varying part of the sensor data, i.e. values measured while the target passes through the measurement area of the sensor. Hence, the constant part of the data should automatically be discarded. It is collected either while the target is outside the sensor's measurement volume or while the robot is not moving. Thus, it is impossible to select the relevant signal parts by simply correlating signal timestamps with the start/ stop timestamps of the robot motion (purple arrows in Fig. 5).

One way to segment the relevant data is to fit piecewise functions. The timestamps at the endpoint of the corresponding function intervals mark the range of the relevant data set

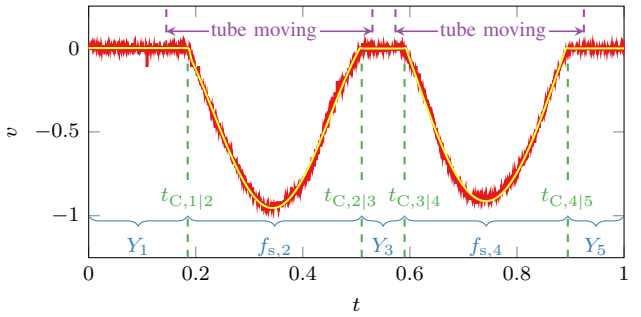

Fig. 5. Normalized sensor readout during calibration motion of a single tube shown in red. $t_{C,k|k+1}$ mark the timestamps at which a change in the sensor readout occurs. Due to hysteresis and possible sensor saturation, $t_{C,k|k+1}$ do not necessarily coincide with the start and stop timestamps of the individual motion sections. The data is split in five sections, each approximated by a piecewise function $(Y_1, f_{s,2}, Y_3, f_{s,4}, Y_5)$ which are combined in a single continuous function plotted in yellow.

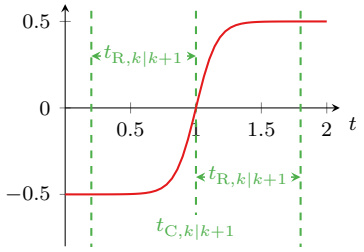

(a) Example blending function $\mathrm{blf}_{k|k+1}$ with $t_{C,k|k+1} = 1$ and $t_{R,k|k+1} = 0.8$.

(b) Parameters used for data approximation

Fig. 6. Blending function and parameters used for data segmentation and measurement data approximation.

(depicted as green lines in Fig. 5). Depending on the chosen piecewise functions, the connection point between successive functions might have a non-smooth derivative. While function fitting under these circumstances can be performed with derivative-free optimization techniques, we show that this problem can also be solved by utilizing gradient-based optimization. Thus, we create an approximation function that is smooth over the entire time domain.

First, the value and time range is normalized to an interval $[0, 1]$. This allows to find start values for the numeric gradient-based optimization which are independent from the magnitude of the sensor readout. For visualization, we shift the sensor data points such that the first value equals 0.

Afterwards, we seek to automatically divide the measurements into five sections indexed by $k \in \{1, 2, 3, 4, 5\}$ (see blue brackets in Fig. 5). The data in every section is approximated by a single function. To create a continuous function over the whole time domain, the piecewise functions of sections k and $k+1$ are blended by a function $\mathrm{blf}_{k|k+1}(t)$:

$$\mathrm{blf}_{k|k+1}(t) = 0.5 \cdot \tanh\left(5 \cdot \frac{t - t_{C,k|k+1}}{t_{R,k|k+1}}\right) \tag{1}$$

with $t_{R,k|k+1}$ being a constant specifying the blending window $t_{C,k|k+1} \pm t_{R,k|k+1}$ as shown in Fig. 6a. Note, that the blending function is centered around $t_{C,k|k+1}$ and that $\mathrm{blf}_k(t_{C,k|k+1} \pm t_{R,k|k+1}) \approx \pm 0.49996$. For approximation of the data in each section k, we either use a constant function $Y_k(t) = Y_k = \mathrm{const.}$ or a general sinusoidal approximation function $f_{s,k}(t)$ which is given by

$$f_{s,k}(t) = A_k \sin\left(\frac{2\pi}{T_k} \cdot t - \frac{\pi}{T_k} \cdot C_k\right) + B_k \tag{2}$$

Here, A_k, B_k, C_k, T_k are constant coefficients influencing the function shape. By utilizing the blending functions, a continuous function f_{cp} over the whole time domain of the measurement is given by

$$\begin{aligned} f_{cp}(t, \boldsymbol{p}) = \; & Y_1 \cdot\big(0.5 - \mathrm{blf}_{1|2}(t)\big) \\ & + \big(0.5 + \mathrm{blf}_{1|2}(t)\big) \cdot f_{s,2}(t) \cdot \big(0.5 - \mathrm{blf}_{2|3}(t)\big) \\ & + \big(0.5 + \mathrm{blf}_{2|3}(t)\big) \cdot \; Y_3 \; \cdot\big(0.5 - \mathrm{blf}_{3|4}(t)\big) \\ & + \big(0.5 + \mathrm{blf}_{3|4}(t)\big) \cdot f_{s,4}(t) \cdot \big(0.5 - \mathrm{blf}_{4|5}(t)\big) \\ & + \big(0.5 + \mathrm{blf}_{4|5}(t)\big) \cdot \; Y_5 \end{aligned} \tag{3}$$

with $t_{R,k|k+1} = t_R = \mathrm{const.}$ and the coefficient vector

$$\begin{aligned} \boldsymbol{p} = [&t_{C,1|2}, t_{C,2|3}, t_{C,3|4}, t_{C,4|5}, \\ &A_2, B_2, C_2, T_2, A_4, B_4, C_4, T_4, Y_1, Y_3, Y_5] \end{aligned} \tag{4}$$

The measurement data is recorded at discrete points in time t_n. Thus, we fit $f_{cp}(t_n, \boldsymbol{p})$ through the measured data points $v(t_n)$ by numerically solving the optimization problem

$$\min_{\boldsymbol{p} \in \mathbb{R}} \sum_n \left(f_{cp}(t_n, \boldsymbol{p}) - v(t_n)\right)^2 \tag{5}$$

The resulting coefficient vector $\boldsymbol{p}$ contains the time spans $[t_{C,1|2}, t_{C,2|3}]$ and $[t_{C,3|4}, t_{C,4|5}]$. They are used to automatically select the data sections relevant for calculating the tubes zero position. Due to normalization of the time and sensor domain, optimal start values necessary for solving (5) can be determined once and then be reused in all further calibration runs.

2) Identification of Tube Reference Position: We define the tube reference position $\alpha_{i,c}$ as the position, where the distance function between tube i and the sensor has an extremum. Depending on the sensing principle, the relation between distance function and sensor readout may be challenging to find. However, an approximation of this function is sufficient, as long as the extrema of both functions align. To determine these functions, we assume, that the target moves along a circular arc with radius r_i as shown in Fig. 6b.

The fitting function depends on the sensing principle of the various sensors. For the inductive and the magnetic sensor, there exists a functional relationship between the sensor readout and the axial distance from the sensor as the sensor is placed below the moving target. By using the relations given in Fig. 6b the distance $d_i(\alpha_i)$ between sensor and target is given by

$$d_i(\alpha_i) = \sqrt{g_i^2 + r_i^2 + 2 \cdot g_i \cdot r_i \sin\left(\alpha_i - \frac{\pi}{2} + \alpha_{i,c}\right)} \tag{6}$$

A typical inductive sensor gives a signal that is proportional to the axial distance of the measurement target. Approximating this distance with d_i, we define the fitting function as $v_{\mathrm{ind},i} \approx k_{\mathrm{ind},i} \cdot d_i(\alpha_i)$.

The magnitude of the spatial magnetic flux density $\boldsymbol{B}$ of a ring magnet at a position s along the magnet's roll axis is given by

$$|\boldsymbol{B}| = B(s) = \frac{B_\mathrm{r}}{2}\left[\frac{H+s}{\sqrt{R_\mathrm{o}^2+(H+s)^2}} - \frac{s}{\sqrt{R_\mathrm{o}^2+s^2}} - \left(\frac{H+s}{\sqrt{R_\mathrm{i}^2+(H+s)^2}} - \frac{s}{\sqrt{R_\mathrm{i}^2+s^2}}\right)\right] \quad (7)$$

with R_i and R_o being the inner and outer diameter of the ring magnet, H its length and B_r its remanence. The Hall sensor fitting function is defined as $v_{\mathrm{hall},i} \approx k_{\mathrm{hall},i} \cdot B\left(d_i(\alpha_i)\right)$.

Electromagnetic tracking provides the position of the tracked target in its own reference coordinate system. However, because the home position is defined in the robot's base frame, the measurements need to be transformed in the desired measurement coordinate system. Ideally, this aligns with the robot base frame. Due to design constraints of the robot's actuation unit, this may not always be feasible. In our setup, we allow it to translate along the y-axis of the robot base coordinate system. With this assumption, the measurement value of the electromagnetic sensor $v_{\mathrm{em},i}$ corresponds to the y-readout of the transformed position data of the electromagnetic tracking device. The fitting function for this value is given by

$$v_{\mathrm{em},i} \approx h_i - r_i \cdot \sin\left(\alpha_i - 0.5\pi - \alpha_{i,\mathrm{c}}\right) \quad (8)$$

with h_i being the distance of the rotation center from the reference coordinate system as shown in Fig. 6b.

Note that due to hysteresis in the tube motions, two function fittings must be performed: One for each time span calculated in section II-D1. Assuming symmetric behavior around the zero position, we use the extrema of these functions ($\alpha_{i,\mathrm{cl}}$ and $\alpha_{i,\mathrm{cr}}$) to calculate the calibration position of tube i by $\alpha_{i,\mathrm{c}} = 0.5 \cdot (\alpha_{i,\mathrm{cl}} + \alpha_{i,\mathrm{cr}})$.

III. EVALUATION

We evaluate the proposed calibration procedure on three different sensor systems (magnetic, inductive and electromagnetic) and compare it to a manual calibration. As *manual calibration* we denote the process of calibration by rotating all tubes to align with the negative y-axis based on visual judgment. This can be seen as the current gold standard for rotational position calibration of CTCR. In our experiment, we seek in determining the reproducibility of the proposed calibration workflow.

A. Experimental setup

Our used CTCR consists of 3 Nitinol tubes with structural parameters as listed in section I-B. Each tube is hold by a collet on a carriage at which bevel gears transform the rotation of two DC motors (RE 25, 20 W, maxon motor AG, Switzerland) into rotational and translational movements of the carriage. Every motor is equipped with a relative position encoder, which gives a resolution of 150 tics/deg and 8960 tics/mm for the rotational and translational degrees of freedom, respectively. A motion control board (DMC-4080, Galil Motion Control, USA) realizes PID control of each motor and provides position data. During calibration the tubes rotate with a speed of 16.7 deg/s.

The calibration procedure is implemented in Matlab (version R2017a, The MathWorks, Inc., USA). All function fittings (see sections II-D1 and II-D2) are solved in a nonlinear least squares manner by using the trust-region-reflective algorithm as implemented in Matlab's `fit` function.

All sensor systems as well as the motion controller provide a timestamp with every data point. After simultaneously triggering the data collection, the sensor and position values are synchronized using Matlab's `synchronize` function.

Depending on the sensing principle, the target material as well as the sensor data used for function fitting (see S-10) vary. The magnetic and the inductive sensor are mounted on a carrier, which is attached to the robot base and can solely be translated along the y-axis to adjust the distance between sensor and target. A close-up of the used targets is depicted in Fig. 1 and the experimental setup is shown in Fig. 7.

1) Magnetic Sensor: The Hall sensor is integrated with an evaluation board (3D Magnetic Sensor 2GO TLE493D-W2B6, Infineon Technologies AG, Germany). Four axial magnetized neodymium ring magnets (N45, outer diameter: 5 mm, inner diameter: 1.5 mm, height: 1 mm) are stacked and used as the target to provide a magnetic field. A field change of 0.13 mT could be detected in a distance up to 35 mm. While the sensor is capable of measuring the magnetic flux density in 3 dimensions, only its magnitude is used as sensor value for calibration. As long as the sensor origin lies inside the base frame's y-z-plane, its orientation can vary because the magnitude of the magnetic flux vector is independent of its orientation in the sensor coordinate system.

2) Inductive Sensor: An inductive sensor (BI8-M18-LIU, Hans Turck GmbH & Co. KG, Germany) with an analog voltage output and a measurement range of up to 5 mm is used. The voltage is approximately linear to the distance between the sensor and an inductive target, which moves along the longitudinal sensor axis. The sensor output is scaled down and converted to a digital signal using an analog digital converter (MCP3008, Microchip Technology Inc, USA). The used target is a steel ring (d_o=10 mm, d_i=1.5 mm, height: 0.9 mm). By placing the longitudinal axis inside the robot's y-z-plane and pointing it in the direction of the point, where the target passes the plane, one can optimize the sensor readout when the tube reaches its zero position. The sensor position can then be adjusted freely to avoid signal saturation during the target motion. We choose to orient the sensor axis in parallel to the robot's y-axis.

3) Electromagnetic Sensor: An electromagnetic tracking coil is inserted into the innermost tube and affixed to the tube tip to serve as target (see Fig. 1(C)). Its position is tracked using a tracking system (Aurora V2, NDI, Canada) which consists of a field generator and a 6 degrees of freedom sensor utilized as reference system. During the calibration procedure,

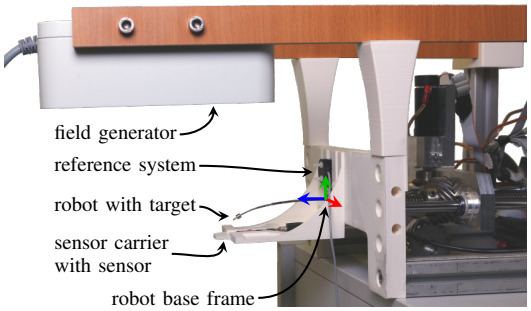

Fig. 7. Experimental setup. The shown sensor carrier with the magnetic sensor can be replaced by the inductive sensor while the field generator and the reference system of the electromagnetic system are permanently attached to the actuation unit. The position of the sensor carrier can only be adjusted along the robot base frame's y-axis.

the position of the coil in the robot tip and the pose of the reference system is measured continuously. The reference system is oriented in the same way as the robot base frame, but slightly shifted along its y-axis. Two bolts fixate it on the robot base plate as shown in Fig. 7, hence its transformation to the robot base frame is known by design. After reading the position of the target coil in the coordinate system of the field generator, it is transformed into the reference coordinate system. The y-value of the target coil position after this transformation is then used as sensor signal. One could also extract the zero position without the help of a reference system. However, this would require more elaborate data processing than presented in II-D2 (e.g. by assuming the target moves in an elliptical orbit).

B. Reproducibility Experiments

Our experiments are composed of four measurement series (one for each sensor as well as the manual calibration) with 10 measurement runs per series (i.e. complete robot calibrations). At the beginning of every series a manual (rough) precalibration is performed which yields the zero reference for the succeeding calibration procedures. All measurement runs of one series relate to this precalibrated position. As reproducibility measure we use the standard deviation σ

$$\sigma = \sqrt{\frac{1}{N-1}\sum_{n=1}^{N}(\alpha_{i,cn} - \bar{\alpha}_{i,c})^2} \tag{9}$$

with N being the number of measurement runs, $\alpha_{i,cn}$ the result of the n-th calibration of tube i and $\bar{\alpha}_{i,c}$ the mean value of the calibrated home position in each series. Therefore, the squared reproducibility measure equals the statistical variance of our experiment. By utilizing the 97.5 % and 2.5 % quantile of the χ^2 distribution with $(N-1)$ degrees of freedom (denoted $\chi^2_{0.975}(N-1)$ and $\chi^2_{0.025}(N-1)$, respectively), the 95 % confidence interval CI of σ is calculated as

$$\mathrm{CI} = \sigma \cdot \sqrt{\left[\frac{N-1}{\chi^2_{0.975}(N-1)}, \frac{N-1}{\chi^2_{0.025}(N-1)}\right]} \tag{10}$$

C. Results

Fig. 8 displays reproducibilities for each tube and sensor system. For tubes 1 and 3 the inductive system shows the smallest values (0.011 ° and 0.067 °), while for tube 2 the electromagnetic system gives the best result (0.04 °). Except for the electromagnetic sensor, σ increases with tube index.

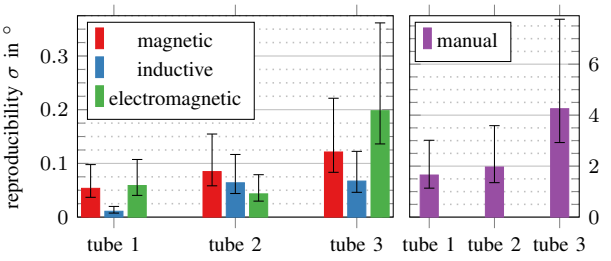

Fig. 8. Reproducibility for each tube. 95 % confidence interval marked by black whiskers. Data for manual calibration is shown with adapted limits.

D. Discussion

It can be observed that the reproducibility is better with increasing tube curvature. A larger curvature results in a larger spatial span of the robot's tip motion for the same rotational distance, which is easier to measure by the sensors.

Overall, our proposed calibration workflow is characterized by high reproducibility. In comparison, the goldstandard (careful manual calibration of the tube's rotational home position) is more than one order of magnitude worse in terms of reproducibility. Furthermore, the 95 % confidence intervals (black whiskers in Fig. 8) of the automated calibration experiments do not overlap with those of the manual calibration, indicating a statistical significant difference. Those rotational offsets for each tube's reference position may cause notable deviations of the tip pose and overall robot shape.

To compare the results of the three sensor systems we perform the F-test [22] on the null hypothesis, that their squared reproducibilities are equal (see Fig. 9). We assume a normal distribution of our measurements and compare the p-values to a significance level of 5 % ($p = 0.05$). This shows, that for tube 1 the high difference between the reproducibility of the inductive sensor and the other two sensor systems is statistically significant. The same conclusion holds for the comparison between the inductive and electromagnetic sensor for tube 3. Regarding all other cases, a greater number of experiments should be performed to rank the sensor systems solely based on their achievable reproducibility.

Calibration with electromagnetic sensor for tube 3 shows the worst reproducibility (especially compared to the results for tube 2 using the same sensor). This indicates, that the function fitting for this set of experiments does not represent the data as precisely as for the other tubes. This is caused by several reasons: The data acquisition and processing rate of the electromagnetic sensor is notably slower than for the magnetic or the inductive sensor (128 ms compared to 32 ms and 4 ms, respectively). Hence, less data points are available for function fitting according to (8). Additionally, the actuation unit contains metallic parts overlapping with the sensing volume of the Aurora system, which may cause additional distortion of the electromagnetic field leading to lower measurement accuracy (see [23]). In combination with the smaller spatial tip movement during calibration of tube 3

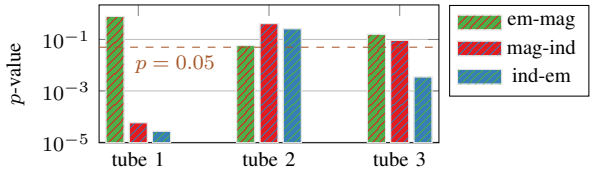

Fig. 9. p-values as calculated by F-test for the null hypothesis, that squared reproducibilities between two measurement series are equal. Compared are calibrations with the electromagnetic (em), magnetic (mag) and inductive (ind) sensor systems. The results are shown on logarithmic scale.

an increased reproducibility error is observed. Yet, this sensor system still outperforms the manual calibration procedure.

All sensors differ in terms of cost and effort to set them up for calibration. The electromagnetic system is the most expensive (several thousand €), followed by the inductive (100-200 €) and the magnetic sensor (<100 €). While the inductive sensor shows the highest reproducibility, special care must be taken to place the sensor in a suitable distance from the target such that all tubes can be calibrated without rearranging the sensor and such that the sensor signal does not saturate during the measurements. This is mostly caused by the very small sensing volume of the system. The electromagnetic sensor eases its positioning due to its comparatively large measurement volume. However, ferromagnetic materials must be removed from this volume. Finally, the magnetic sensor system shows a good compromise between measurement accuracy and applicable sensing volume.

Therefore, we conclude that the proposed calibration procedure is very well suited to achieve a reproducible rotational home position for CTCR.

IV. CONCLUSION

We introduce a method for joint level calibration of CTCR, which allows for the automatic identification of the rotational zero position for each tube. To the best of our knowledge, this is the first automated Level 1 calibration step for CTCR. By evaluating the methodology with three different sensor systems (based on electromagnetic, inductive and magnetic sensing principles) we show, that our approach provides significant improvement in terms of reproducibility of the determined calibration position compared to a manual calibration.

In future work, hardware integration into the actuation unit of a CTCR could reduce placement variations occuring while mounting the sensor system. By integrating the target directly into application specific tools, the calibration process could be fused more seamlessly with the application workflow. Furthermore, we seek to evaluate our approach on CTCR with non-constant precurvature and to analyze the effect of parameters like tube rotation rate and sensor rate on the calibration result. Lastly, combining our joint level calibration method with geometric calibration has the potential to further increase the achievable accuracy of CTCR, which is key to applications with higher levels of autonomy.

ACKNOWLEDGMENT

We thank Andreas Waiz for his help with experiments and sensor selection as well as Eduard Popp for his assistance in performing the sensitivity analysis.

REFERENCES

[1] K. Schröer, "Precision and Calibration," in *Handbook of Industrial Robotics*, S. Y. Nof, Ed. Hoboken, NJ, USA: John Wiley & Sons, Inc., 1999, ch. 39, pp. 795–810.
[2] A. C. Majarena, J. Santolaria, D. Samper, and J. J. Aguilar, "An Overview of Kinematic and Calibration Models Using Internal/External Sensors or Constraints to Improve the Behavior of Spatial Parallel Mechanisms," *Sensors*, vol. 10, no. 11, pp. 10 256–10 297, 2010.
[3] G. Antonelli, S. Chiaverini, and G. Fusco, "A calibration method for odometry of mobile robots based on the least-squares technique: theory and experimental validation," *IEEE Transactions on Robotics*, vol. 21, no. 5, pp. 994–1004, 2005.
[4] G. Robinson and J. Davies, "Continuum robots - a state of the art," in *IEEE International Conference on Robotics and Automation*, vol. 4, 1999, pp. 2849–2854.
[5] J. Burgner-Kahrs, D. C. Rucker, and H. Choset, "Continuum Robots for Medical Applications: A Survey," *IEEE Transactions on Robotics*, vol. 31, no. 6, pp. 1261–1280, 2015.
[6] R. Grassmann, V. Modes, and J. Burgner-Kahrs, "Learning the Forward and Inverse Kinematics of a 6-DOF Concentric Tube Continuum Robot in SE(3)," in *International Conference on Intelligent Robots and Systems*, no. 3. IEEE, 2018, pp. 5125–5132.
[7] Z. Roth, B. Mooring, and B. Ravani, "An overview of robot calibration," *IEEE Journal on Robotics and Automation*, vol. 3, no. 5, pp. 377–385, 1987.
[8] C. Escande, T. Chettibi, R. Merzouki, V. Coelen, and P. M. Pathak, "Kinematic Calibration of a Multisection Bionic Manipulator," *IEEE/ASME Transactions on Mechatronics*, vol. 20, no. 2, pp. 663–674, 2015.
[9] M. Dehghani and S. A. A. Moosavian, "Characteristics identification of continuum robots for exact modeling," in *IEEE RSI/ISM International Conference on Robotics and Mechatronics*, 2013, pp. 26–31.
[10] B. Deutschmann, T. Liu, A. Dietrich, C. Ott, and D. Lee, "A Method to Identify the Nonlinear Stiffness Characteristics of an Elastic Continuum Mechanism," *IEEE Robotics and Automation Letters*, vol. 3, no. 3, pp. 1450–1457, 2018.
[11] L. Wang and N. Simaan, "Geometric calibration of continuum robots: Joint space and equilibrium shape deviations," *IEEE Transactions on Robotics*, vol. 35, no. 2, pp. 387–402, 2019.
[12] M. T. Chikhaoui, S. Lilge, S. Kleinschmidt, and J. Burgner-Kahrs, "Comparison of Modeling Approaches for a Tendon Actuated Continuum Robot With Three Extensible Segments," *IEEE Robotics and Automation Letters*, vol. 4, no. 2, pp. 989–996, 2019.
[13] R. J. Webster, J. M. Romano, and N. J. Cowan, "Kinematics and calibration of active cannulas," in *IEEE International Conference on Robotics and Automation*, 2008, pp. 3888–3895.
[14] R. J. Webster, J. Romano, and N. Cowan, "Mechanics of Precurved-Tube Continuum Robots," *IEEE Transactions on Robotics*, vol. 25, no. 1, pp. 67–78, 2009.
[15] D. C. Rucker, R. J. Webster III, G. S. Chirikjian, and N. J. Cowan, "Equilibrium Conformations of Concentric-tube Continuum Robots," *The International Journal of Robotics Research*, vol. 29, pp. 1263–1280, 2010.
[16] C. Greiner-Petter and T. Sattel, "On the influence of pseudoelastic material behaviour in planar shape-memory tubular continuum structures," *Smart Materials and Structures*, vol. 26, no. 12, p. 125024, 2017.
[17] A. Saltelli, S. Tarantola, F. Campolongo, and M. Ratto, *Sensitivity Analysis in Practice*. Chichester, UK: John Wiley & Sons, Ltd, 2002.
[18] D. C. Rucker, B. A. Jones, and R. J. Webster, "A geometrically exact model for externally loaded concentric-tube continuum robots," *IEEE Transactions on Robotics*, vol. 26, no. 5, pp. 769–780, 2010.
[19] P. E. Dupont, J. Lock, B. Itkowitz, and E. Butler, "Design and control of concentric-tube robots," *IEEE Transactions on Robotics*, vol. 26, no. 2, pp. 209–225, 2010.
[20] H. B. Gilbert, R. J. Hendrick, and R. J. Webster III, "Elastic stability of concentric tube robots: A stability measure and design test," *IEEE Transactions on Robotics*, vol. 32, no. 1, pp. 20–35, 2016.
[21] J. Lock and P. E. Dupont, "Friction modeling in concentric tube robots," in *IEEE International Conference on Robotics and Automation*, 2011, pp. 1139–1146.
[22] R. E. Walpole, R. H. Myers, S. L. Myers, and K. E. Ye, *Probability and Statistics for Engineers and Scientists*, 9th ed. Prentice Hall, 2012.
[23] S. R. Kirsch, C. Schilling, and G. Brunner, "Assesment of metallic distortions of an electromagnetic tracking system," in *Medical Imaging 2006: Visualization, Image-Guided Procedures, and Display*, vol. 6141. SPIE, 2006, pp. 143 – 151.